Materials Advances

ROYAL SOCIETY OF CHEMISTRY

PAPER

View Article Online
View Journal | View Issue

Cite this: *Mater. Adv.*, 2024, 5, 5231

Insulin-infused bimetallic nano-subclusters as a multifunctional agent for ROS scavenging, antibacterial resilience, and accelerated *in vitro* cell migration†

Deepinder Sharda[a] and Diptiman Choudhury *[ab]

This is the first report on the synthesis and wound healing application of green synthesized insulin-infused bimetallic (copper–silver) nano-subclusters (ICu–AgNSCs) with high stability, aqueous solubility, biocompatibility, and target specificity. HRTEM and SAED data confirm octahedral particles (with a diameter of 9.6 ± 2.2 nm) composed of discrete copper clusters on the periphery and a silver core that are further infused with an insulin corona (0.5 ± 0.2 nm), as confirmed by the characteristics of Cu–OH and Ag–O stretching bonds and alteration in insulin amide bonds. The ICu–AgNSCs had high insulin loading efficiency (93.90 ± 1.05%) and a high drug release rate (92.69 ± 0.90% within 40 h), making them ideal for sustained release applications. Wound healing in diabetic conditions gets delayed due to the prolonged proinflammatory phase and microbial infestation, which may lead to clinical amputation. Therefore, advanced therapeutics that promote cell growth by reducing inflammation and microbial growth are required. ICu–AgNSCs may satisfy all these criteria. Insulin and quercetin have ROS scavenging and anti-inflammatory properties. Insulin and copper have cellular growth-promoting activity; additionally, silver has antimicrobial properties. ICu–AgNSCs have been shown to accelerate diabetic cell migration *in vitro*, making them an ideal choice for pre-clinical and clinical applications.

Received 16th March 2024,
Accepted 4th May 2024

DOI: 10.1039/d4ma00278d

rsc.li/materials-advances

1. Introduction

Wound healing is a significant challenge for the scientific community despite all the available treatments, and the global expenditure on healing wounds ranges from $28.1 to $96.8 billion.[1] Healing is a complex event involving overlapping phases, which work together against the damage and restore the lost tissue or organ.[2] Healing begins with hemostasis, which involves the activation of platelets, clot formation, and matrix organization. In proliferation, the accumulation of growth factors, connective tissues, and angiogenesis factors occurs at the wound site. In the inflammatory phase, the proinflammatory cytokines promote vasodilation and activate the different signaling pathways. The resynthesis of the extracellular matrix occurs in the remodeling phase to maintain the balance between dead and live cells.[3,4] However, certain factors disrupt the normal physiological mechanism of wound healing, including microbial infection, trauma, ischemia, and diabetes mellitus,[5,6] which can be avoided by preventing bacterial infestation, removing the dead tissue and debris, and keeping the wound moist.[7] In diabetes, there is persistent release of proteases, proinflammatory cytokines, reactive oxygen species, and low secretion of anti-inflammatory cytokines.[8] Diabetic wounds are more susceptible to infection due to the body's immune response impairment.[6] The activity of different antioxidant enzymes, including glutathione peroxidase and superoxide dismutase, is reduced, which leads to damage by free radical generation.[9] Diabetes also affects protein synthesis, re-epithelialization, cell migration, and proliferation of fibroblasts and keratinocytes by preventing the transport of nutrients to the wound site.[10,11] Reactive oxygen species (ROS) generation is also a major issue as their accumulation prevents the efficient functioning of macrophages and endogenous stem cells. Also, ROS causes endothelial dysfunction and restricts angiogenesis.[12] Additionally, ROS generation due to bacterial infection leads to chronic wound infection by damaging endothelial cells and blood vessels.[13,14]

To promote healing, tremendous research is going on to develop novel formulations that are biocompatible, efficient, environment-friendly, and cost-effective. Here, the role of nanoparticles comes into play as they possess massive potential in

[a] *Department of Chemistry and Biochemistry, Thapar Institute of Engineering and Technology (TIET), Patiala-147004, Punjab, India*
[b] *Center of Excellence in Emerging Materials (CEEMS), Thapar Institute of Engineering and Technology, Patiala, Punjab-147004, India. E-mail: diptiman@thapar.edu; Tel: +91-8196949843*

† Electronic supplementary information (ESI) available. See DOI: https://doi.org/10.1039/d4ma00278d

diverse fields ranging from drug delivery to bioimaging and wound healing, with anticancer, antimicrobial, and antioxidant activities.[15,16] Many nano-formulations using gold, silver, copper, zinc, and cobalt were developed to study their wound healing, antibacterial and antioxidant properties.[17–19] Recently, protein-based metallic nanoparticles have gained enormous interest because of their target specificity, biodegradability, ability to alter their surface for efficient attachment of the drugs, and easily metabolizable nature.[20] Protein-modified nanoformulations are developed using different proteins, including bovine serum albumin, insulin, transferrin, lactoferrin and silk fibroin.[21] All these formulations possess single metal ions and, thus, obtain the properties of those constituent metal ions only. This makes them less effective and unstable, and they tend to form aggregates, gradually decreasing their potential activities. However, the need of the hour is to develop formulations with multiple activities to increase their efficacy. Bimetallic formulations are preferred over monometallic because they can enhance multiple properties depending upon their surface effect, quantum tunneling effect, and quantum size effect.[22] They also possess outstanding potential in diverse biomedical applications.[23,24] Based on the arrangement of the metal atoms, bimetallic particles can be classified into four major categories: alloyed, intermetallic, subclusters, and core–shell.[25] Bimetallic nano-subclusters (BNSCs) are a fascinating class of nanomaterials composed of two distinct metal atoms having two separate phases and a shared interface.[26] BNSCs exhibit properties that make them attractive candidates for various applications in catalysis, sensing, and biomedicine. Their ability to encapsulate and deliver therapeutic agents directly to targeted cells offers a promising approach to improving drug treatment's efficacy while minimizing side effects.[27] Additionally, BNSCs can be functionalized with targeting ligands to enhance their specificity and selectivity towards specific cell types.[28] In this work, we report the synthesis of novel insulin-coated silver–copper bimetallic nano-subclusters having a potential role in promoting cell migration and antioxidant and antibacterial activities.

Silver enhances the differentiation of fibroblasts into myofibroblasts, which promote proliferation and keratinocyte relocation, thus increasing wound contraction. Silver activates macrophages, modulates the inflammatory response, reduces scar formation, and exhibits antimicrobial, anti-inflammatory, and antioxidant activities.[29,30] Furthermore, the oxidation of silver leads to the generation of free radicals and reactive oxygen species (ROS), both of which are capable of damaging the biomolecules, including DNA, lipids, and proteins, along with intracellular organelles including mitochondria, ribosomes, vacuoles, *etc.* in the microbes.[31] Copper promotes wound healing by modulating the secretion of various cytokines and growth factors. It stimulates the expression of fibrinogen, collagen, and integrin, which are present in the extracellular matrix and are essential for the attachment of cells to the extracellular matrix. It also exhibits biocidal action.[32,33] Copper regulates vascular endothelial growth factor (VEGF), which is essential for forming new blood vessels.[34] It enhances the expression of hypoxia-induced factor-1-alpha (HIF-1α), which promotes angiogenesis and skin regeneration.[35] Furthermore, quercetin has a massive role in wound healing, as it promotes fibroblast proliferation and migration, decreases the proinflammatory cytokines, reduces the immune cell infiltration, increases the collagen fiber accumulation, and improves the GSH level along with vascular endothelial growth factor, fibroblast growth factor, and alpha-smooth muscle actin levels. Quercetin itself acts as a reducing and stabilizing agent for synthesizing multiple nanoparticles.[36,37] Insulin is gaining colossal interest from researchers for its ability to act as a growth factor and to transition the proinflammatory cytokines to anti-inflammatory cytokines, which are essential for inflammation, re-epithelialization, wound repair, and regeneration.[38,39] It promotes protein and lipid biosynthesis, stimulates cell glucose uptake, increases cellular differentiation, and promotes cellular migration.[40] After binding to the receptors, insulin activates different pathways like Akt, Erk, and NRF-2 pathways to promote wound healing.[41,42] The insulin-templated nanoformulations have promising potential for bioimaging, super-resolution microscopy, and wound healing.[39,43]

Here, we have synthesized the bimetallic nanosubclusters to check the synergism between silver nanoparticles and insulin-loaded copper quantum clusters for healing wounds when linked together to yield formulations in the nano-range. To maintain the affected individual's quality of life, there is a need to explore potent and effective agents that not only have effective drug delivery potential but also have antimicrobial and antioxidant potency to yield better outcomes without making the process cumbersome, costly, and risky for the patient's life.

2. Materials and methods

2.1 Chemicals and the cell line

Silver nitrate ($AgNO_3$), copper sulfate ($CuSO_4$), formaldehyde, HCl, NaOH, and H_2O_2 were of analytical grade and were purchased from HiMedia, India. Recombinant human insulin was purchased from Elli Lilly, India. For cell culture, DMEM cell culture media, Fetal Bovine Serum (FBS), 100× penicillin–streptomycin, and phosphate buffered saline (PBS) having pH 7.4 were purchased from HiMedia, India. Human primary epithelial keratinocytes (HEKa cells) ATCC-PCS-200-011 were procured from Himedia, India. The cells were cultured, maintained, and treated with DMEM containing 5% FBS at 37 °C and 5% CO_2. The bacterial strains used for investigating antibacterial activity include *Escherichia coli* (MTCC no. 448), *Bacillus subtilis* (MTCC no. 441), *Acinetobacter calcoaceticus* (MTCC no. 1948), and *Staphylococcus aureus* (MTCC no. 902), which were procured from IMTech, Chandigarh, India.

2.2 Synthesis of bimetallic nano-subclusters

At first, the insulin-protected copper quantum clusters (ICuQCs) were prepared by following a previously reported one-pot method. The insulin solution with a final

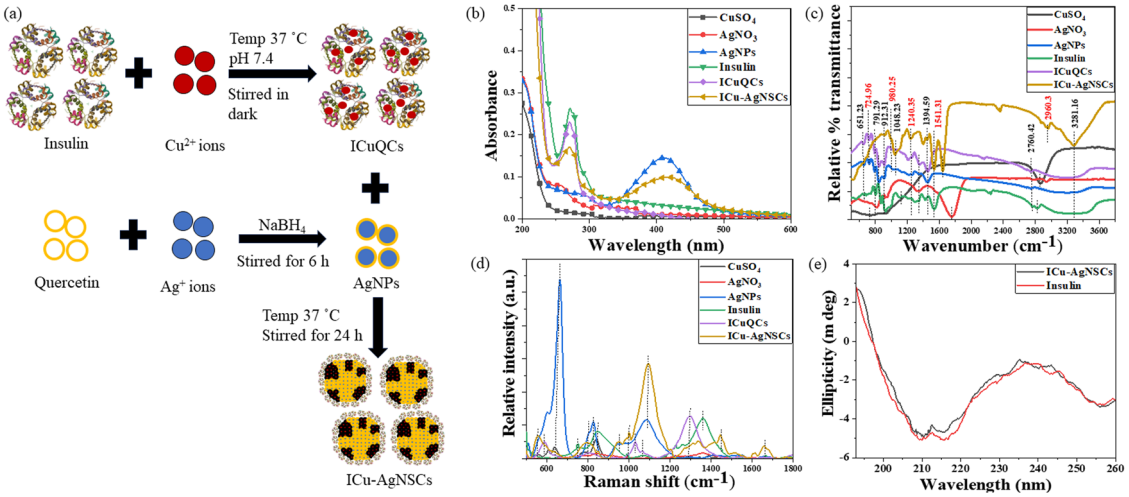

Fig. 1 Synthesis and spectroscopic studies confirming the interactions between ICuQCs and AgNPs for synthesizing ICu–AgNSCs. (a) Schematic representation of the synthesis protocol being followed for formulating bimetallic nanosubclusters. (b) UV-visible absorption spectra showing the peak of pure insulin, ICuQCs, and ICu–AgNSCs at ~272 nm and a peak at ~412 nm for AgNPs and ICu–AgNSCs, confirming the interaction between the two. (c) FTIR spectra of $CuSO_4$, $AgNO_3$, AgNPs, insulin, ICuQCs and ICu–AgNSCs in the range of 400–4000 cm^{-1}, indicating the formation of new bonds; Cu–OH stretching and the Ag–O bond, which were otherwise not present in pure insulin. (d) Raman spectra of $CuSO_4$, $AgNO_3$, AgNPs, insulin, ICuQCs and ICu–AgNSCs indicate the involvement of different functional groups of insulin in synthesizing ICu–AgNSCs. (e) Circular dichroism confirms the stability of secondary protein structure with minimal changes even after the synthesis of ICu–AgNSCs.

concentration of 1.82 mM was prepared, and using NaOH solution (0.1 M), its pH was adjusted to 10.5 and kept in the dark. Afterward, a salt solution ($CuSO_4 \cdot 5H_2O$) of the same concentration was prepared, followed by mixing insulin and salt solution in 1 : 1, which was further followed by adjustment of the pH of the final solution to a physiological pH of 7.4, using HCl (0.1 N). The resulting solution was kept in the incubator at slow stirring (240 rpm) for 24 h at 37 °C. The final solution was dialyzed using a 10 kDa cut-off dialysis membrane, stored at 4 °C. After that, silver nanoparticles (AgNPs) were prepared to have the same concentration using quercetin and by slightly modifying the previously reported method[44] and incubated in the dark with the earlier formed insulin copper quantum clusters for 24 h at 37 °C to obtain the bimetallic nano-subclusters (ICu–AgNSCs) as shown in Fig. 1a. Then, the final solution was again dialyzed using a 10 kDa cut-off dialysis membrane, stored at 4 °C, and used further for characterization and biological studies.

2.3 Study of interactions using spectroscopic techniques

Initially, to monitor the interactions between the AgNPs and ICuQCs to form ICu–AgNSCs, UV-visible absorbance studies were done by using the UV-2600 spectrophotometer (Shimadzu), which was operated between 200 and 800 nm, and a 4000 μl quartz cuvette having a path length of 1 cm was used to determine the absorbance of both the salt solutions ($CuSO_4$ and $AgNO_3$), AgNPs, insulin, ICuQCs, and insulin linked bimetallic nano-subclusters (ICu–AgNSCs).

To study the metal–protein interactions of the ICu–AgNSCs, FTIR was performed using an Agilent Cary 600 series spectrophotometer. The potassium bromide (KBr) method was used to prepare the sample pellets. The sample scanning was done from 400 cm^{-1} to 4000 cm^{-1} to monitor the changes in certain specific bonds.

Furthermore, the same samples were analyzed using surface enhanced Raman scattering (SERS) spectroscopy to study the structural changes in insulin protein. All the samples were prepared on a silicon wafer ten minutes before the measurement. The samples were scanned from 500 cm^{-1} to 1800 cm^{-1}. The LabRam Hr Evolution Horiba, equipped with a detector and microscope, was used to record the Raman spectra of insulin and ICu–AgNSCs at 785 nm.

Furthermore, circular dichroism (CD), the most reliable technique, was used to monitor the stability of secondary protein structures after the interactions between protein molecules and metallic nanoparticles. The CD studies were performed at 25 °C with 1 ml of the sample in the 200–260 nm wavelength range for pure insulin and ICu–AgNSCs using phosphate buffer (pH 7.4) as a solvent with a Mos500 CD BioLogic instrument.

2.4 Study of particle size and morphology and elemental analysis

DLS analysis (dynamic light scattering) was done using a Malvern DLS-Zeta size analyzer to determine the hydrodynamic size of synthesized ICu–AgNSCs. Thereafter, to find out the morphology and size of bimetallic nanosubclusters, high-resolution transmission electron microscopy (HRTEM) (Talos F200S G2, Thermo Scientific) was used. For this, the samples were centrifuged at 240 rpm for 15 minutes, and then the pellet was thoroughly washed to remove the unbound metal salt or impurities associated with the sample. Furthermore, the sample pellet was subjected to elemental mapping to find out the distribution of metal salts in the sample and to determine the

percentage of the elements present by using the Energy dispersive X-ray spectrometer (EDS) (Bruker QUANTAX 200).

2.5 Drug loading and release kinetics

To monitor the drug loading in the nanosubclusters, 1 ml of the synthesized ICu–AgNSCs was centrifuged for 15 min at 6000 rpm. The supernatant and the pellet were collected to determine the amount of bind and free drug and, thus, determine the drug loading capacity of the formulations. After that, the release kinetics were investigated to determine the amount of insulin released from the nanosubclusters and, thus, determine the drug delivery efficiency. 1 ml of the synthesized nanosubclusters was taken, placed in a dialysis membrane, and kept under slow stirring conditions (250–300 rpm). The drug release was measured at specific time intervals for 40 hours under physiological conditions of pH 7.4 and a temperature of 37 °C. The absorption values (at 595 nm) were later plotted to determine the trend of drug release using BSA standard curves.

2.6 *In vitro* studies

2.6.1 Cell viability. For evaluating the cell viability of synthesized nanosubclusters, the MTT (3-(4,5-dimethylthiazol-2-yl)-2,5-diphenyltetrazolium bromide) assay was performed by using the HEKa cell line (human epidermal keratinocytes, adult). The HEKa cells were grown in a cell culture plate and let to reach a confluency of up to 80–85%, followed by their splitting, and seeded into 96 well plates, with each well having the density of cells as 1×10^4. After that, the cells were placed in the incubator for further cell growth and to reach a confluency of up to 80–85%, and the medium was regularly changed after specific time intervals. When the plate became confluent, the different samples, including salt solutions, AgNPs, ICuQCs, and ICu–AgNSCs, having different concentrations (5, 10, 20, and 40 μM) were added in sets of 3 to get three concordant readings. The plate was later incubated for 24 hours at a temperature of 37 °C and 5% CO_2. After 24 h, the medium in the MTT plate was replaced with fresh medium with MTT (2 mg ml^{-1} in 5% ethanol) and incubated for another 3 h. Following the specified time interval, the medium was again discarded and replaced with 200 μl of dimethyl sulfoxide (DMSO) for dissolving the formazan crystals. Finally, the absorbance was checked at a wavelength of 575 nm. The equation used to calculate the percentage of cell viability is as follows:

$$\%\ \text{cell viability} = \left[\left(\frac{A_t}{A_c}\right) \times 100\right]\% \quad (1)$$

Here, A_t is the absorbance of the test substance and A_c is the absorbance of the control solvent for each concentration.

2.6.2 Effect of ICu–AgNSCs on the cell migration *in vitro* determined using phase contrast imaging. To study the effect of synthesized formulations on cell migration *in vitro*, the HEKa cell line was used and grown in 60 mm plates both in the absence and presence of glucose (360 mg dl^{-1}) to monitor the changes in normal and diabetic conditions. The cells were grown in the DMEM-F12 medium (FBS-free medium) and kept in a humidified incubator at 37 °C and 5% CO_2. The cells were allowed to grow until they reached a confluency of 80–85%, followed by creating a scratch in the confluent plate using a sharp object such as the sterile 200 μl tip to analyze the effect on cell migration using the scratch assay. The plates were later incubated with fixed concentrations (5, 10, 20, and 40 μM) of different samples, including salt solutions, AgNPs, ICuQCs, and ICu–AgNSCs. Time-lapse imaging was done to monitor the changes in the scratch diameter, and the variation in the scratch width was measured after 6 h, 12 h, and 24 h, respectively. The width was measured at different positions of the scratch-made in each plate. The mean of those independent readings of scratch diameter is taken to calculate the percentage change in cell migration in the normal and diabetic conditions individually.

2.6.3 Antioxidant activity against H_2O_2-induced cytotoxicity. To investigate the antioxidant activity, HEKa cells were seeded in 96 well plates and maintained at 37 °C and 5% CO_2 for 24 hours in the DMEM medium supplemented with 10% FBS and let to reach 85–90% confluency. Afterward, the cells were divided into two sets and treated with varying concentrations of H_2O_2 (0, 50, 100, 200, 400, 800, 1200, 1600, and 2000 μM) in DMEM for a brief period of 1 hour, and later the cells were washed twice with PBS to obliterate H_2O_2. The cells in one of the sets were incubated with fresh DMEM medium alone, and in the other set, the cells were treated with bimetallic nanosubclusters of fixed concentrations alongside DMEM (40 μM) and kept in the incubator for 24 hours. Following this, an MTT assay was performed to determine the effect on cell viability after treatment with H_2O_2 and to study the antioxidant effect of the synthesized nanosubclusters on cell viability. The medium was discarded, and the cells were washed with PBS before adding fresh medium containing MTT and kept for a 3-hour incubation period, followed by treatment with DMSO to measure the absorbance at 570 nm.[45]

2.6.4 Detection of ROS using DCFDA. ROS generation was determined by flow cytometry using DCF-DA staining. The Heka cells were grown in the DMEM medium and treated with varying concentrations of H_2O_2 (200, 1000, and 4000 μM) for a brief period of 1 hour. Then, the medium containing H_2O_2 was discarded, and the cells were treated with bimetallic nanosubclusters (40 μM) for 12 hours after adding fresh medium. Following this, the cells were detached using trypsin–EDTA solution and suspended in 0.5 ml of PBS, to which DCFDA (10 μM) was added 10 minutes before performing flow cytometry analysis.

2.7 Antibacterial activity of synthesized ICu–AgNSCs. To determine the antibacterial activity of the synthesized nanoformulations, the Minimum Inhibitory Concentration (MIC) was determined. MIC is the minimum concentration at which an antibacterial agent retains the bacterial growth inhibition for the defined period. The growth curve experiment was performed using the Gram-negative (*Escherichia coli* and *Acinetobacter calcoaceticus*) and Gram-positive (*Bacillus subtilis* and *Staphylococcus aureus*) bacteria to determine the MIC of synthesized formulations. The

microdilution method was performed to determine the antimicrobial activity using 96 well plates as per previously reported methods. Initially, the bacteria were cultivated in the LB broth medium at 37 °C, and after 24 hours, the bacteria were taken in the LB medium, and the concentration was adjusted to 10^{-8} CFU ml^{-1}. To evaluate the antimicrobial activity of nanosubclusters, we added 20 μl of bacteria, 20 μl of nanosubclusters (ranging from 0.5 μM to 64 μM), and 160 μl of Luria Broth in each well of 96 well plates. The negative control is considered in the last well as inoculated broth without nanosubclusters. The plates were kept in a microplate shaker for 24 hours and 37 °C under slow shaking conditions. Following this, the best concentration of synthesized nanosubclusters against different bacteria is determined by the MIC method. Furthermore, the IC_{50} values were determined along with the MIC value for each bacterium.[46]

2.8 Determination of the combination index (CI) for $AgNO_3$ and ICuQCs

The combination index (CI) is one of the quantitative measures used to calculate the effect of different drugs in combination with one another. The drug combination index was estimated when investigating synergistic or antagonistic drug combinations to quantify the level of synergism or antagonism. If the value of the combination index is less than 1 (CI < 1), it indicates that different drugs, when administered together, work together to promote each other's activity, called the synergistic effect. When the CI value is equal to 1 (CI = 1), it indicates that none of the two drugs interfere with each other's action, hence exhibiting the additive effect, and a CI value of greater than 1 (CI >1) shows the inhibitory activity of one drug on the other drug, thus called the antagonistic effect. To calculate the combination index, the cell viability of HEKa cells was determined at different concentrations of $AgNO_3$ and ICuQCs, and then calculations were done using the following equation (eqn (2)).

$$\mathrm{CI} = \frac{(D)1}{(D_x)1} + \frac{(D)2}{(D_x)2} \quad (2)$$

where

$$D_x = D_{m}\left[\frac{f_a}{f_u}\right]\frac{1}{m} \quad (3)$$

Here, $(D)1$ and $(D)2$ denote the respective concentrations of silver nitrate and insulin copper quantum clusters. The median effect equation (eqn (3)) is used for the determination of single drug concentrations giving the same effect $(D_x)1$ and $(D_x)2$. Here, f_a and f_u denote the cell fractions that are affected and unaffected, respectively, and are equal to $10^{(y-\text{intercept})/m}$, where m represents the slope median in the median effect plot of $\log(D)$ *vs.* $\log(f_a/f_u)$.[47]

2.9 Statistical analysis

The data here are represented as mean ± SD of at least three independent experiments. The statistical data analysis was done in MS excel using one-way ANOVA. The corresponding *p*-values were calculated to check if the data were statistically significant or not.

3. Results and discussion

3.1 Spectroscopic analysis

3.1.1 Spectroscopic changes determined using absorbance spectra after synthesis of ICu–AgNSCs. After synthesizing ICu–AgNSCs, their spectroscopic characterization was done to observe the absorbance spectra of the formed nanosubclusters. After analysis of AgNPs and insulin, the absorbance spectra of AgNPs indicate a peak-maximum at 412 nm having an absorbance value of 0.145, and for insulin without any added salt solution, we obtained a sharp peak at 271.61 nm with an absorbance value of 0.262, both of which are in accordance with the work reported. The absorbance spectra obtained for ICuQCs exhibit an absorption maximum at 271.31 nm, having an absorbance value of 0.23, whereas after incubating the AgNPs with ICuQCs for 48 h, two distinct absorption maxima were obtained at 271.31 nm and 412.86 nm, having absorbance values of 0.16 and 0.10, respectively, indicating the interaction between the two, which confirms the synthesis of ICu–AgNSCs as shown in Fig. 1b.

3.1.2 FTIR and Raman spectra for monitoring the interactions between the protein and metal ions after the formation of nano-subclusters. To monitor the variation in the functional groups of insulin after interactions between the insulin copper quantum clusters and silver nanoparticles, FTIR was performed for $CuSO_4$, $AgNO_3$, AgNPs, insulin, ICuQCs, and ICu–AgNSCs. The slight variations in major protein peaks appeared at different wavenumbers due to intermolecular interactions of ICuQCs and AgNPs and are shown in Fig. 1c. The peak at 791.29 cm^{-1} and 651.23 cm^{-1} indicates the NH_2 stretching and C═S stretching, respectively, in AgNPs, insulin, ICuQCs, and ICu–AgNSCs.[40] Then, peaks at 724.96 cm^{-1} for $CuSO_4$ and at 718.19 cm^{-1} for ICuQCs and ICu–AgNSCs indicate Cu–OH stretch.[48] Ag–O stretching was observed for $AgNO_3$, AgNPs, and ICu–AgNSCs at 946.16 cm^{-1}, 986.79 cm^{-1}, and 980.25 cm^{-1} respectively.[49] In addition to these, peaks at 912.31 cm^{-1} and 845.34 cm^{-1} for AgNPs, at 925.85 cm^{-1} for insulin, at 912.31 cm^{-1} and 838.57 cm^{-1} for ICuQCs and at 912.31 cm^{-1} for ICu–AgNSCs show the C–O stretching, confirming the interaction between AgNPs and ICuQCs.[39] Peaks at 1113.20 cm^{-1} for insulin and 1048.23 cm^{-1} for ICu–AgNSCs show C–N stretching.[40] Amide III stretching was observed for insulin and ICuQCs and ICu–AgNSCs at 1207.25 cm^{-1} and 1240.23 cm^{-1} respectively. NO_3 symmetric and asymmetric stretch was observed in $AgNO_3$ at 1320.86 cm^{-1}, in AgNPs at 1341.17 cm^{-1}, in insulin at 1307.31 cm^{-1}, in ICuQCs at 1347.51 cm^{-1} and at 1394.59 cm^{-1} in ICu–AgNSCs, respectively.[50] C–OH stretching was observed at 1448.32 cm^{-1} in AgNPs and ICuQCs, at 1420.83 cm^{-1} in insulin, and at 1441.24 cm^{-1} in ICu–AgNSCs.[38] Amide II, C═O stretch was observed at 1535.29 cm^{-1} in insulin and at 1541.31 cm^{-1} in

Table 1 The comparative wavenumber values indicated by FTIR in the range of 400–4000 cm^{-1} for $CuSO_4$, $AgNO_3$, AgNPs, insulin, ICuQCs, and ICu–AgNSCs, showing the positions of different functional groups present, which determine the interaction amongst AgNPs and ICuQCs, indicating the formation of bimetallic nanoparticles

Functional group	$CuSO_4$	$AgNO_3$	AgNPs	Insulin	ICuQCs	ICu–AgNSCs	Ref.
Amine NH stretch	—	—	—	3281.16	3281.16	3281.16	39
Amide-B –CH stretch	—	—	—	2827.15	—	2960.32	40
–OH stretch	2860.25	2760.42	2760.42	2760.42	2760.42	2867.03	38
Nitrile stretch	—	—	—	2247.81	2160.53	2351.64	40
N═O stretching	—	1755.74	—	—	—	1642.13	50
Amide II C═O stretch	—	—	—	1535.29	—	1541.31	38
C–OH stretch	—	—	1448.32	1420.93	1448.32	1441.24	38
NO_3 symmetric and asymmetric stretch	—	1320.86	1341.17	1307.31	1347.51	1394.59	50
Amide III stretching	—	—	—	1207.25	1207.25	1240.35	50
C–N stretch	—	—	—	1113.20	—	1048.23	40
Ag–O stretching	—	946.16	986.79	—	—	980.25	49
C–O stretch	—	—	912.31 845.34	925.85	912.31 838.57	912.31	39
NH_2 stretch	—	791.29	791.29	791.29	791.29	791.29	40
–Cu–OH stretch	724.96	—	—	—	718.19	718.19	48
C═S stretch	—	—	651.23	651.23	651.23	651.23	40

ICu–AgNSCs.[38] N═O stretching was observed at 1755.74 cm^{-1} in $AgNO_3$ and at 1642.13 cm^{-1} in ICu–AgNSCs.[50] Nitrile stretch was marked at 2247.81 cm^{-1}, 2160.53 cm^{-1}, and 2351.64 cm^{-1} in insulin, ICuQCs, and ICu–AgNSCs respectively.[40] A broad peak of –OH stretch was observed for all the formulations between 2760.42 cm^{-1} and 2867.03 cm^{-1}.[38] Amide B C–H stretch was observed at 2827.15 cm^{-1} and 2960.32 cm^{-1}, respectively, in insulin and ICu–AgNSCs.[40] The amine N–H stretch was observed in insulin, ICuQCs, and ICu–AgNSCs at 3281.16 cm^{-1}.[39] The comparative wavenumbers of each solution are given in Table 1.

Similarly, Raman spectral analysis was used to study the significant conformational changes in insulin after interaction with metal ions. The S–S stretch was observed at 598.10 cm^{-1}, 584.76 cm^{-1}, and 554.24 cm^{-1}, respectively, in AgNPs, ICuQCs and ICu–AgNSCs.[51] The band at 662.45 cm^{-1} is observed for $AgNO_3$, AgNPs, ICuQCs, and ICu–AgNSCs, indicating a C–S–C bond.[52] The bands at 793.13 cm^{-1} for $CuSO_4$ and ICuQCs and at 794.12 cm^{-1} for ICu–AgNSCs indicate the Cu–OH stretching.[48] The C–H out-of-plane wagging was observed at 847.81 cm^{-1} in $CuSO_4$ and insulin, at 841.74 cm^{-1} in $AgNO_3$ and ICuQCs, at 828.70 cm^{-1} in AgNPs and 849.74 cm^{-1} in ICu–AgNSCs.[52] The Ag–O stretching was observed at 947.26 cm^{-1} in AgNPs and ICu–AgNSCs and at 931.12 cm^{-1} in $AgNO_3$.[49] The C–O–C bond was observed at 986.23 cm^{-1} in insulin and ICu–AgNSCs.[40] The peaks at 995.87 cm^{-1}, 970.38 cm^{-1}, and 1002.69 cm^{-1} for insulin, ICuQCs, and ICu–AgNSCs, respectively, indicate the C–C stretching.[53] C–N stretching was observed in AgNPs, insulin, ICuQCs, and ICu–AgNSCs, respectively, at 1086.86 cm^{-1}, 1071.15 cm^{-1}, 1072.34 cm^{-1} and 1097.53 cm^{-1}.[54] Amide III (α-helix) was observed at 1229.43 cm^{-1} in insulin and ICu–AgNSCs.[55] The band for Amide III random coils was observed at 1283.37 cm^{-1} for insulin, 1301.75 cm^{-1} for ICuQCs, and 1311.24 cm^{-1} and 1340.28 cm^{-1} for ICu–AgNSCs.[56] The C–H bend was observed at 1364.12 cm^{-1} in ICu–AgNSCs.[40] The peak for Amide II was observed at 1442.80 cm^{-1} and 1445.50 cm^{-1}, respectively, for insulin and ICu–AgNSCs.[20] The peak at 1516.32 for insulin,

Table 2 The comparative wavenumber values indicated by Raman spectra in the range of 500–1800 cm^{-1} for $CuSO_4$, $AgNO_3$, AgNPs, insulin, ICuQCs, and ICu–AgNSCs showing the positions of different functional groups present, which determine the interaction amongst AgNPs and ICuQCs, indicating the formation of bimetallic nanoparticles

Functional group	$CuSO_4$	$AgNO_3$	AgNPs	Insulin	ICuQCs	ICu–AgNSCs	Ref.
Amide-I	—	—	—	1658.21	—	1606.23 1658.21	20
C–C stretch	—	—	—	1516.32	1516.32	1516.32	40
Amide-II	—	—	—	1442.80	—	1445.50	20
C–H bend	—	—	—	—	—	1364.12	40
Amide-III (random coils)	—	—	—	1283.37	1301.75	1311.24 1340.28	56
Amide III (α helix)	—	—	—	1229.43	—	1229.43	55
C–N stretching	—	—	1086.86	1071.15	1072.34	1097.53	54
C–C stretching	—	—	—	995.87	970.38	1002.69	53
C–O–C	—	—	—	986.23	—	986.23	40
Ag–O stretching	931.12	—	947.26	—	—	947.26	49
C–H out of plane wagging	847.08	841.74	828.70	847.81	841.74	849.74	52
Cu–OH stretch	793.13	—	—	—	793.13	794.12	48
C–S–C stretching vibrations	—	662.45	662.45	—	662.45	662.45	52
S–S stretch	—	—	598.10	—	584.76	554.24	51

ICuQCs, and ICu–AgNSCs indicates the C–C stretch.[40] The peaks for Amide I were observed at 1658.21 cm^{-1} for insulin and ICu–AgNSCs and at 1606.23 cm^{-1} for ICu–AgNSCs alone[20] and are shown in Fig. 1d. The comparative wavenumbers of each solution are mentioned in Table 2.

Circular dichroism was performed using the insulin protein and ICu–AgNSCs to monitor the stability of the secondary structure of protein after interaction with metal ions from silver nanoparticles and insulin copper quantum clusters. The three significant far UV signals were observed for both solutions. A positive peak was observed at ~194 nm (representative of the β-sheet), and two negative peaks, one at ~208 nm and the other at ~217 nm, were observed (representative of the α-helix), indicating the secondary structure of insulin protein.[57] Slight variations in all three peaks were observed for ICu–AgNSCs, that is, 5.57%, 3.75%, and 5.15%, respectively, and are shown in Fig. 1e. The % variation is much less when compared with pure insulin, confirming protein stability with no significant observable structural changes.

3.2 Structure, composition, and stoichiometry of metal insulin nanosubclusters

The hydrodynamic sizes of AgNPs, ICuQCs, and ICu–AgNSCs were measured and found to be 25 ± 5 nm, 35 ± 5 nm, and 40 ± 5 nm, respectively, as shown in Fig. S1a–c (ESI) respectively. Furthermore, the formation of nearly octahedral bimetallic nano-subclusters (ICu–AgNSCs) having a size of 9.6 ± 2.2 nm and an outer insulin layer (0.5 ± 0.2 nm) was confirmed by transmission electron microscopic images (at scales of 20 and 2 nm) as shown in Fig. 2a and b, respectively, and the SAED pattern obtained is shown in Fig. 2c. Additionally, the lattice fringes in HRTEM were spaced apart by 0.23 nm and 0.17 nm and were indexed with Ag(111) and Cu(200) respectively. It was found that copper is mainly present in the peripheral region, and silver is inside, forming distinct phases with copper. Furthermore, it was evident from the percentages obtained for Ag and Cu in the nanoparticles (7.63% and 6.17%) that silver is in higher amounts, which is further confirmed by the TEM image, where the electron-dense portion indicates copper

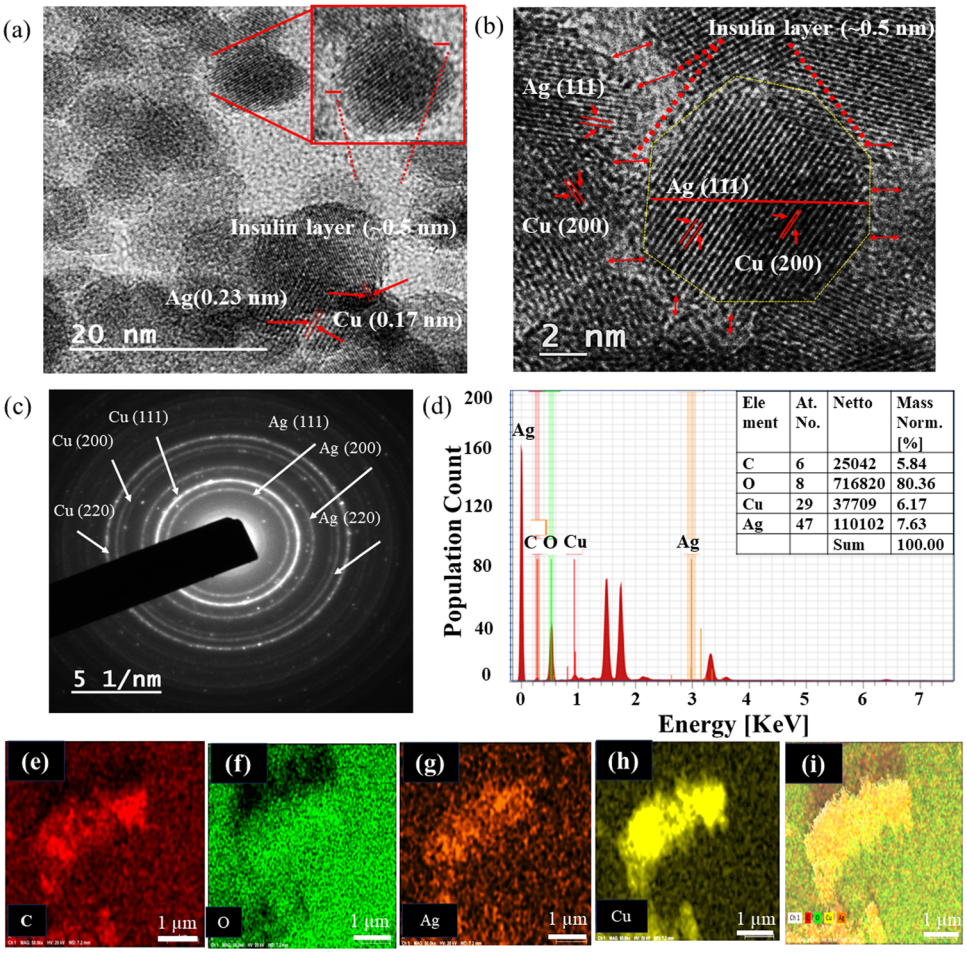

Fig. 2 Structural, morphological, and elemental characterization of ICu–AgNSCs. TEM micrographs of ICu–AgNSCs show the nanoparticle size to be ~9.6 ± 2.2 nm at scales of (a) 20 nm and (b) 2 nm (inset shows the insulin layer of 0.5 ± 0.2 nm around individual bimetallic clusters). (c) SAED confirms the crystalline structure of bimetallic nanosubclusters. (d) EDS spectra show the presence of both silver and copper (inset shows the relative percentage of each element). Elemental mapping showing the different elements in ICu–AgNSCs: (e) carbon, (f) oxygen, (g) silver, (h) copper, and (i) the combined image showing all elements.

and the rest of the part is for silver having lower electron density. Energy-dispersive X-ray spectroscopy was used for the determination of different elements, including C, O, Cu, and Ag, in the bimetallic nano-subclusters as shown in spectra given in Fig. 2d. Elemental mapping was done to verify the presence of both silver and copper in the synthesized bimetallic nano-subclusters, and it confirms the presence of carbon (Fig. 2e), oxygen (Fig. 2f), silver (Fig. 2g), copper (Fig. 2h) and a combination of all elements, as shown in Fig. 2i.

3.3 Drug loading and release kinetics studies

The synthesized bimetallic nanosubclusters were studied for their drug loading and release kinetics, and the encapsulation efficiency of insulin in the bimetallic nanosubclusters was determined to be 88.54 ± 0.40%. For the initial 8 h, burst drug release was observed, followed by sustained drug release after that, with most of the drug being released in 40 h. Furthermore, the percentage of drug released from ICu–AgNSCs by the end of 40 hours was found to be 93.90 ± 0.90%, making it an efficient drug delivery system, and is shown in Fig. 3a and the drug released per hour in mg ml^{-1} is shown in Fig. 3b.

3.4 *In vitro* cell studies

3.4.1 HEKa cell viability assay. Cell viability analysis was performed using HEKa cells and MTT assay to monitor the biocompatibility of the synthesized formulations. The study was performed using salt solutions, silver nanoparticles, insulin, insulin copper quantum clusters, and bimetallic nanoformulations at four different concentrations of each (5, 10, 20, and 40 μM). The cell viability of untreated cells (control) is taken as 100, and the values for the rest of the samples are compared with that of the control. The cells treated with $CuSO_4$ exhibit the cell viabilities of 100.57 ± 1.77%, 102.22 ± 3.74%, 105.58 ± 3.81%, and 107.05 ± 5.09% and the cells treated with $AgNO_3$ have the cell viabilities of 100.85 ± 6.73%, 102.45 ± 1.39%, 106.37 ± 1.38%, and 108.07 ± 4.12% at 5, 10, 20, and 40 μM respectively. The cells treated with AgNPs have cell viability on the order of 109.12 ± 6.01%, 115.07 ± 3.93%, 117.89 ± 1.66%, and 119.78 ± 2.48%. The cells after treatment with insulin show viabilities of 121.29 ± 3.74% at 5 μM, 124.72 ± 2.06% at 10 μM, 128.45 ± 5.35% at 20 μM and 132.39 ± 2.47% at 40 μM respectively. The cells exposed to ICuQCs have higher viabilities than those exposed to insulin alone and are 124.47 ± 2.78%, 127.18 ± 1.04%, 131.96 ± 5.11%, and 135.18 ± 2.96%, respectively, at 5, 10, 20, and 40 μM respectively. Cell viability after treatment with bimetallic ICu–AgNSCs showed much more significant changes, which are 133.07 ± 1.18% at 5 μM, 150.37 ± 1.04% at 10 μM, 163.92 ± 3.76% at 20 μM and 169.72 ± 0.38% at 40 μM respectively, and is shown in Fig. 3c and comparative data are shown in Table S1 (ESI). From the graph, it was demonstrated that none of the samples was toxic to the cells. Moreover, as the concentration

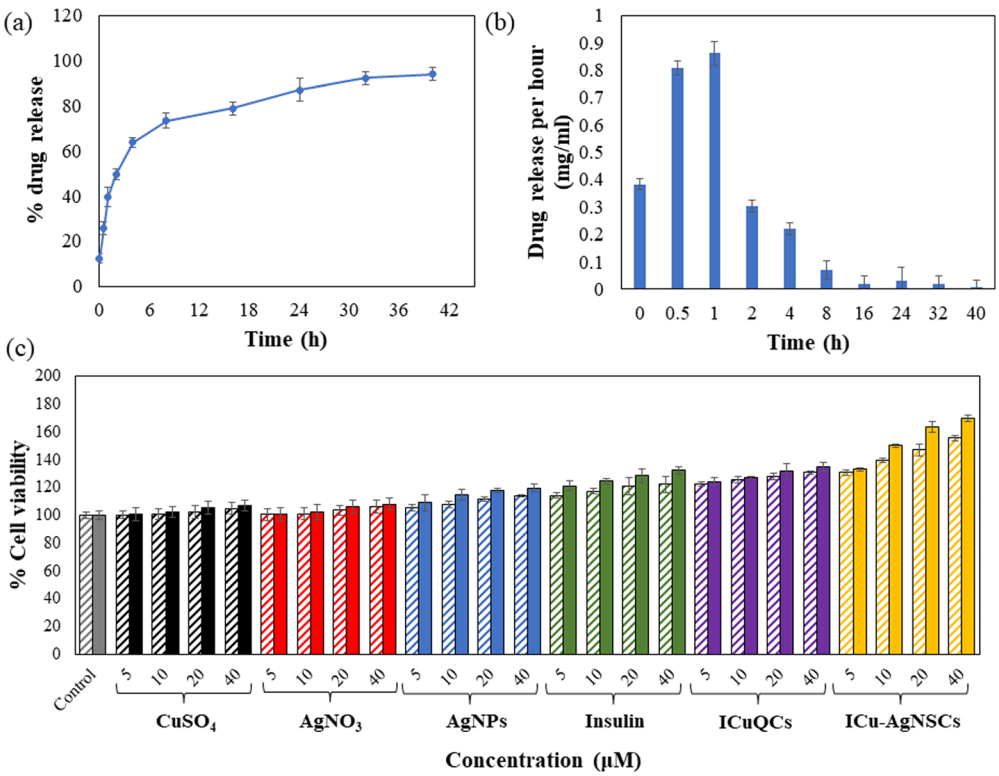

Fig. 3 Drug release kinetics and cell viability assay. (a) The plot showing the release kinetic studies to determine the % drug released from the bimetallic nanosubclusters. (b) The drug released per hour in mg ml^{-1} from ICu–AgNSCs. (c) MTT assay to determine the effect of synthesized formulations on the cell viability to determine their potential role in cell growth and wound healing. The data were plotted as the mean value of three independent experiments, and the solid bars indicate normal conditions, while the patterned bars indicate diabetic conditions in the graph.

of added samples increases, the cell viability increases and is found to be maximum for synthesized bimetallic ICu–AgNSCs, indicating that nano-subclusters formed to promote cell division and growth and thus can be used as a potent material for wound healing.

3.4.2 HEKa cell migration assay in diabetic and normal conditions. The synthesized bimetallic nanoformulations, along with silver nitrate salt solution, copper sulfate solution, silver nanoparticles, insulin, and insulin quantum clusters, were tested for their potential role in cell migration in normal and diabetic conditions on HEKa cells by treating them with a fixed concentration of each one of them (40 μM). The bimetallic nanosubclusters demonstrate excellent migration abilities in both conditions but have a more migration impact in normal conditions than the diabetic ones. As time passes, a significant increase in cell division eventually leads to enhanced migration rates when monitored after specific time intervals. Initially, the percentage change in the scratch diameter is measured in HEKa cells taken as control (without any treatment) after 6, 12, and 24 h and is shown in Fig. 4(a)(a–c). Following this, we observed the changes in cells grown in diabetic conditions. The percentage changes in the scratch diameter of cells treated with $CuSO_4$ after 6, 12, and 24 h are 0.56 ± 0.39%, 1.40 ± 0.46%, and 1.30 ± 0.37%, respectively, and are shown in Fig. 4(a)(d–f). Similarly, the percentages of a gap left in cells that were treated with $AgNO_3$ were found out to be 0.28 ± 0.43%, 0.35 ± 0.50%, and 0.86 ± 0.44%, respectively, after fixed intervals (Fig. 4(a)(g–i)). The % changes in migration after 6, 12, and 24 h in the presence of AgNPs and insulin are even higher and are found out to be 25.30 ± 1.35%, 45.18 ± 0.63%, and 46.29 ± 0.43% in the presence of AgNPs (Fig. 4(a)(j–l)) and 39.81 ± 0.37%, 50.87 ± 0.18%, and 52.17 ± 0.51% for cells incubated with insulin (Fig. 4(a)(m–o)). For cells after treatment with ICuQCs, the values of % change in scratch are 44.75 ± 0.25%, 56.14 ± 0.35%, and 58.69 ± 0.35%, respectively (Fig. 4(a)(p–r)). The maximum change in the scratch diameter as compared with control is observed in cells treated with the synthesized bimetallic formulations, where the values are found out to be 65.52 ± 0.51%, 72.28 ± 0.01%, and 75.21 ± 0.44% after 6, 12, and 24 h (Fig. 4(a)(s–u)). A comparative study of variation in the scratch diameter of the diabetic cells after treating the cells with all samples is shown graphically in Fig. 4(a)(v).

The exact concentration and time intervals were followed to monitor the scratch diameter variation under normal conditions. The percentage variation in the scratch diameter in control cells is shown in Fig. 4(b)(a–c). The % changes in the scratch diameter after treatment with $CuSO_4$ are 1.54 ± 0.46%, 2.59 ± 0.46%, and 1.38 ± 0.44% (Fig. 4(b)(d–f)) and after treatment with $AgNO_3$ are 1.85 ± 0.32%, 2.22 ± 0.49%, and

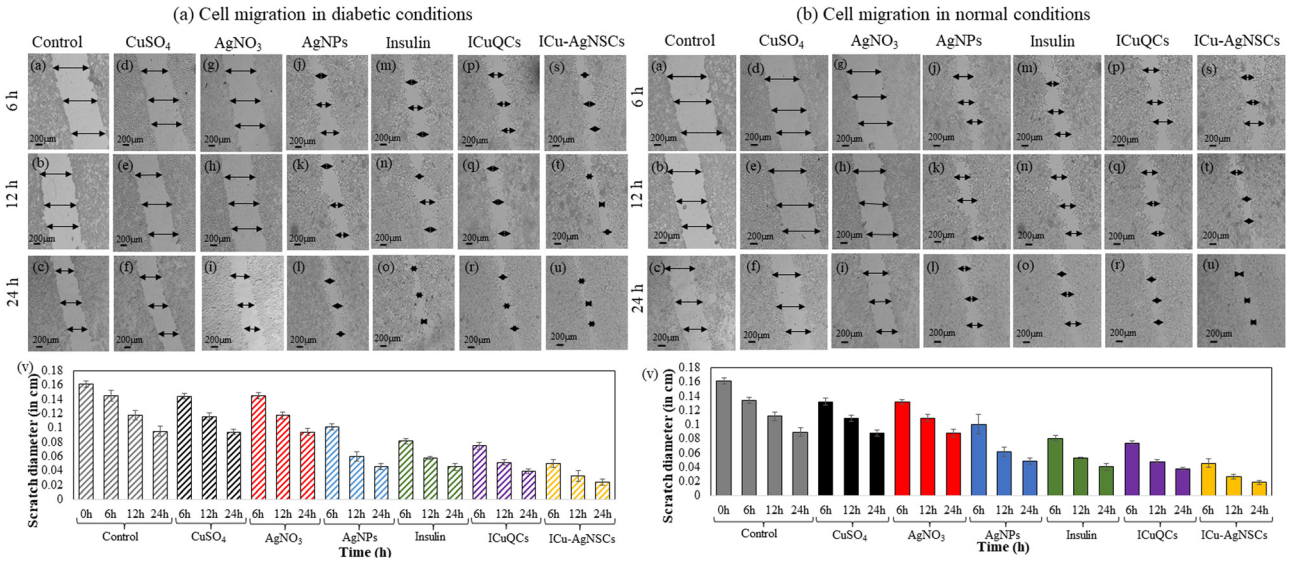

Fig. 4 Promotion and monitoring of *in vitro* cell migration in the diabetic and normal cells using ICu–AgNSCs. The bimetallic nano-subclusters induced better cell migration in HEKa cells compared to salt solutions, insulin, AgNPS, and ICuQCs. The cells were incubated with a fixed concentration of all the solutions, that is, 40 μM. HEKa cells were taken as control (without any added formulations). (a) The figure shows cell migration in diabetic conditions using HEKa cells without any treatment: (a) 6 h, (b) 12 h, and (c) 24 h; the cells treated with the salt solution of copper sulfate after (d) 6 h, (e) 12 h and (f) 24 h; the HEKa cells after treatment with silver nitrate: (g) 6 h, (h) 12 h and (i) 24 h; the cells after treating them with silver nanoparticles: (j) 6 h, (k) 12 h and (l) 24 h; cells after treatment with insulin after a duration of (m) 6 h, (n) 12 h and (o) 24 h respectively; cells treated with ICuQCs after (p) 6 h, (q) 12 h and (r) 24 h and cells after treatment with ICu–AgNSCs after (s) 6 h, (t) 12 h and (u) 24 h. (v) The plot shows the relative change in cell migration in diabetic conditions after treatment with all the solutions respectively after specific time intervals. (b) The figure shows cell migration in normal conditions using HEKa cells without any treatment: (a) 6 h, (b) 12 h, and (c) 24 h; the cells treated with the salt solution of copper sulfate after (d) 6 h, (e) 12 h and (f) 24 h; the HEKa cells after treatment with silver nitrate: (g) 6 h, (h) 12 h and (i) 24 h; the cells after treating them with silver nitrate are shown in figures after (j) 6 h, (k) 12 h and (l) 24 h; cells after treatment with insulin after a duration of (m) 6 h, (n) 12 h and (o) 24 h respectively; cells treated with ICuQCs after (p) 6 h, (q) 12 h and (r) 24 h and cells after treatment with ICu–AgNSCs after (s) 6 h, (t) 12 h and (u) 24 h. (v) The plot shows the relative change in cell migration in normal conditions after treatment with all the solutions respectively after specific time intervals.

1.85 ± 0.55% respectively (Fig. 4(b)(g–i)). For the cells treated with AgNPs, insulin, and ICuQCs, the % variations in migration with time is more as compared to those treated with the salt solutions alone and are equal to 29.91 ± 0.44%, 49.47 ± 0.64%, and 51.73 ± 0.42% for AgNPs (Fig. 4(b)(j–l)), 43.87 ± 0.35%, 52.59 ± 0.14% and 54.62 ± 0.50% for insulin alone (Fig. 4(b)(m–o)) and 48.43 ± 0.37%, 57.40 ± 0.25% and 58.33 ± 0.21% for ICuQCs (Fig. 4(b)(p–r)). The bimetallic nanosubclusters exhibit the maximum % changes in the scratch diameter, which are 66.04 ± 0.61%, 76.66 ± 0.31%, and 79.62 ± 0.31%, respectively, indicating the enormous potential of prepared nanosubclusters for enhanced cell migration in normal conditions (Fig. 4(b)(s–u)). The graph in Fig. 4(b)(v) shows the variation in the normal scratch diameter as a comparative study of all the formulations after particular time intervals. A comparative data table of change in cell migration in normal and diabetic cells is shown in Table S2 (ESI). To find the statistical significance of data, p values were calculated for scratch assay in diabetic and normal conditions, and the comparative data are shown in Table S3 (ESI).

3.4.3 Antioxidant activity against H_2O_2 induced cytotoxicity. H_2O_2, when present in biological samples or cells, is widely responsible for its cytotoxic effect. As per previous studies, H_2O_2 is toxic to the cells (HEKa) at a concentration of 400 μM or higher and eventually causes a decrease in the cell viability with increasing concentration. The same effect was observed in this study. When treated only with H_2O_2 with a concentration of 400 μM or higher, cell viability was decreased due to the cytotoxic nature of H_2O_2 responsible for the free radical generation as shown in Fig. 5a. On the other hand, when the cells initially treated with 1000 μM H_2O_2 were incubated with varying concentrations (5, 10, 20, and 40 μM) of synthesized bimetallic formulations, an antioxidant effect was observed due to the scavenging of H_2O_2-induced reactive oxygen species responsible for cell death as shown in Fig. 5b. The ICu–AgNSCs increase the scavenging of ROS and the % scavenging goes on increasing with increase in the concentration of ICu–AgNSCs, making them potent H_2O_2 scavengers essential for promoting the antioxidant activity of nano-subclusters. The ROS scavenging percentages after treatment with 5, 10, 20, and 40 μM of ICu–AgNSCs are 6.76 ± 1.98%, 14.85 ± 1.40%, 21.72 ± 3.56%, and 28.37 ± 1.31%, respectively.

3.4.4 Intracellular ROS measurement. Flow cytometry was performed to examine the ROS scavenging activity of synthesized nanoformulations. Briefly, the non-fluorescent DCFDA dye exhibits green fluorescence when it comes into contact with ROS-generating species and it is determined by measuring the fluorescence at 572 nm using flow cytometry. Initially, the analysis was done on control cells and cells containing only the DCFDA dye. After that, the ROS scavenging activity of

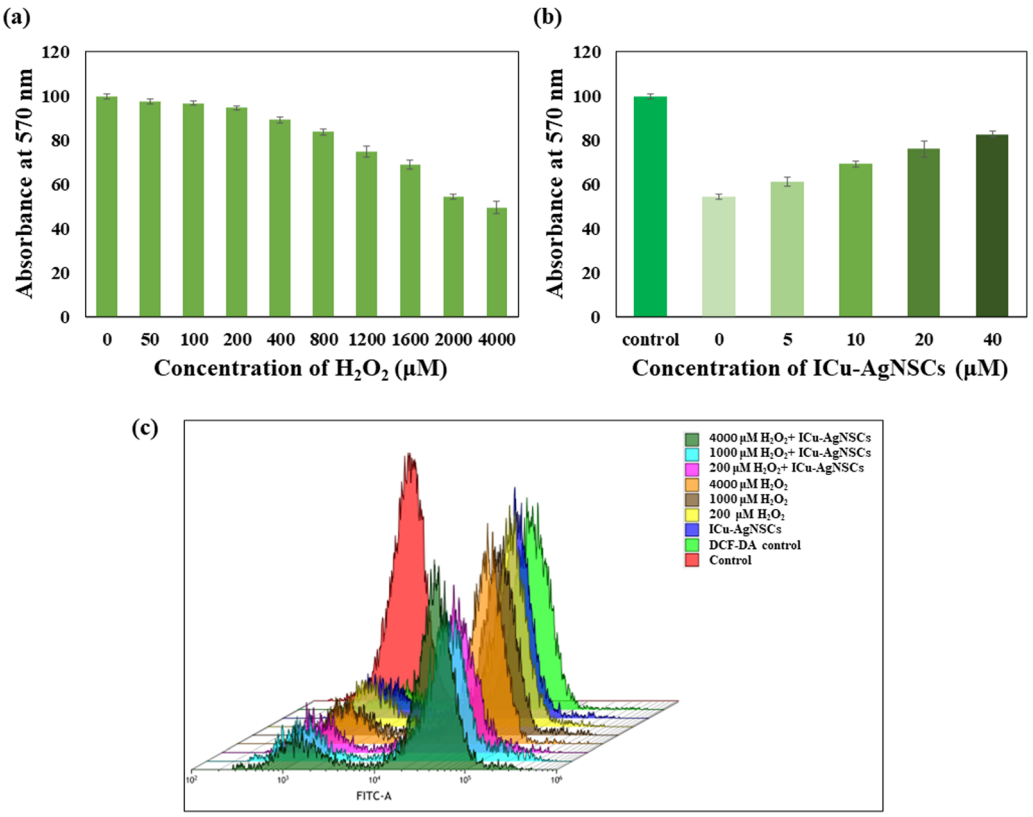

Fig. 5 Reactive oxygen species scavenging potential of ICu–AgNSCs. (a) Effect of varying concentrations of H_2O_2 mediated ROS on the cell viability of HEKa cells. (b) ROS scavenging effect of varying concentrations of ICu–AgNSCs against H_2O_2 mediated ROS. Fluorescence microscopy to monitor the intracellular ROS scavenging by ICu–AgNSCs in HEKa cells. (c) Flow cytometry analysis of ROS scavenging in the presence of varying concentrations of bimetallic nanosubclusters.

bimetallic nanosubclusters was determined, for which initially, the fluorescence was measured for the cells treated with varying concentrations of H_2O_2 followed by the cells treated with bimetallic nanosubclusters. The results show prominent scavenging of H_2O_2-induced ROS in the presence of ICu–AgNSCs. The percentage variation in fluorescence is measured with respect to DCFDA control cells. The percentage increase in ROS after treatment with 4000, 1000, and 200 μM of H_2O_2 is found to be 22.81%, 38.56%, and 47.05% respectively. The cells, after treatment with ICu–AgNSCs (40 μM), showed a sharp decline in the fluorescence intensity, which is 28.40% and 21.78%, respectively, for 1000 and 4000 μM H_2O_2, which is in agreement with the ROS scavenging data obtained in the previous section, and a higher decrease was observed in cells treated with lowest concentration of H_2O_2, which is 200 μM, which is even 1.76% less than DCFDA control itself, indicating the strong ROS scavenging potential of synthesized formulations, which is very beneficial for promoting the wound healing by overcoming the ROS as shown in Fig. 5(c).

3.5 Antibacterial effect on Gram-positive and Gram-negative strains

The antibacterial activity was investigated using the broth dilution method, and the MIC and IC_{50} values against each bacterium were determined. The MIC value for both Gram-negative bacteria, *Escherichia coli*, and *Acinetobacter calcoaceticus*, is found out to be 16 μM and is shown in Fig. 6a and b, and for Gram-positive bacteria, including *Bacillus subtilis* and *Staphylococcus aureus*, the MIC value is 64 μM, which is shown in Fig. 6c and d. The possible reason behind this is due to the easy influx of small nanoparticles into the cell wall of Gram-negative bacteria, which consists of a unique outer membrane and a single peptidoglycan layer as compared with the Gram-positive bacteria having multiple peptidoglycan layers, which makes the entry of nanoparticles difficult into the bacterial membrane. The IC_{50} values for *E. coli*, *A. calcoaceticus*, *B. subtilis*, and *S. aureus* are 5.11 ± 1.52 μM, 4.85 ± 0.43 μM, 5.153 ± 1.25 μM, and 4.91 ± 1.75 μM, respectively, indicating the influential role of nanosubclusters in the antibacterial activity as shown in Fig. 6e and f.

3.6 Combination index of silver nanoparticles and insulin copper quantum clusters

To calculate the CI, D_m was calculated using m and y from Fig. S2a (ESI) for AgNPs and Fig. S2b (ESI) for ICuQCs. The calculated CI values for AgNPs and ICuQCs indicate a synergistic effect between the two, as the calculated values by varying the concentrations of these two formulations are found out to be less than one, indicating that the two formulations enhance each other's activity when combined. These results are in accordance with the ones obtained from MTT assay for cell viability and scratch assay for cell migration studies, indicating

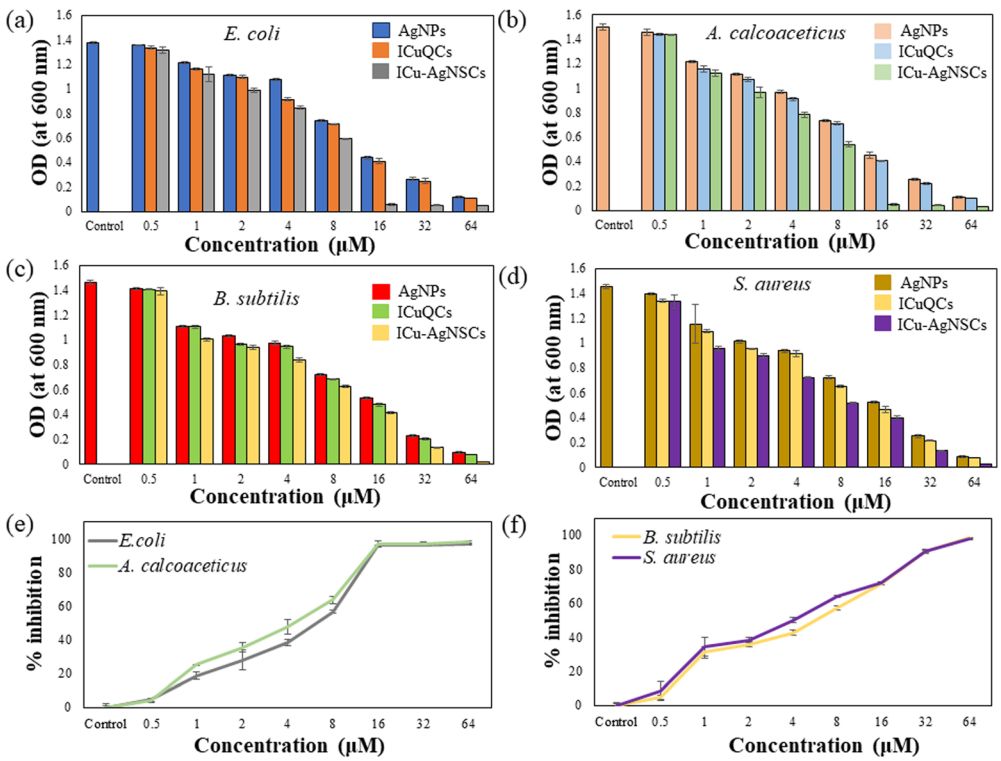

Fig. 6 Monitoring the antibacterial activity against Gram-negative and Gram-positive bacteria using AgNPs, ICuQCs, and ICu–AgNSCs. (a) Antibacterial activity against *E. coli*. (b) Antibacterial activity against *A. calcoaceticus*. (c) Antibacterial activity against *B. subtilis*. (d) Antibacterial activity against *S. aureus*. (e) % bacterial inhibition against Gram-negative *E. coli* and *A. calcoaceticus* using ICu–AgNSCs. (f) % bacterial inhibition against Gram-positive *B. subtilis* and *S. aureus* using ICu–AgNSCs.

their potential role in wound healing applications. The data are shown in Table S4 (ESI†).

4. Conclusion

Maintaining an efficient microenvironment across the wound site is critical to avoid microbial contamination and eliminate all possible complications that can hinder wound recovery, thus lowering healthcare costs and increasing life quality. Effective wound healing agents that are biocompatible and target-specific and have a high drug delivery rate are always required. We synthesized the bimetallic nano-subclusters by combining the silver nanoparticles and insulin copper quantum clusters to study their potential role in accelerating cell migration in normal and diabetic conditions, antioxidant role, and antimicrobial activity. Insulin is widely known for its role in promoting cellular growth by decreasing the blood glucose level, exhibiting the antioxidant effect and modulating the inflammatory responses by replacing the proinflammatory cytokines with the anti-inflammatory cytokines. Silver and copper have been explored for decades for their antimicrobial potential, which is essential for faster and contamination-free wound healing. Insulin and quercetin possess anti-inflammatory and antioxidant activities. Depending upon these features, the formulations were synthesized and checked for synergistic effects in normal and diabetic conditions.

The synthesized nanosubclusters are the first of their kind, having two distinct metal ions embedded in the protein corona, and exhibited a desirable HRTEM size of about 9.6 ± 2.2 nm and demonstrated notable encapsulation efficiency and drug release profile. By efficiently conjugating the insulin copper quantum clusters and silver nanoparticles, the targeted delivery was obtained due to the enormous presence of insulin receptors across the human cells, which gives them an upper hand over general formulations. The FTIR and Raman spectra show the intermolecular interaction between metal ions and insulin and exhibit moderate structural changes in the amide regions of the protein. Also, the stability of the protein secondary structure was maintained throughout the synthesis, which was confirmed by CD spectroscopy. The MTT assay and the combination index analysis performed on the silver nanoparticles and insulin copper quantum clusters emphasized the significant synergistic effect between the two, eventually resulting in better cell migration abilities with antioxidant and antibacterial activities of synthesized subclusters. Furthermore, the synthesized bimetallic nanosubclusters exhibited accelerated cell migration properties in normal and diabetic conditions, even at very low concentrations. Apart from this, the subclusters possess antioxidant and antibacterial properties, which are essential for promoting microbial infection-free wound recovery.

Thus, the remarkable cell migration potential, antibacterial activity, and antioxidant properties of these novel bimetallic nanosubclusters make them highly potential candidates for their further use in biomedical applications and exploration of *in vivo* applications. It is our hope that the outcomes of this paper will promote further research on the development of bimetallic nanosubclusters, which have enormous potential for normal and diabetic wound healing and can be further explored for *in vivo*, pre-clinical, and clinical studies.

Conflicts of interest

The authors declare no conflicts of interest.

Acknowledgements

DC is willing to thank CEEMS and the Indian Council of Medical Research (ICMR) Govt of India for funding (project no. 17X(3)/Adhoc/63/2022-ITR, 17X(3)/Adhoc/3/2022-ITR). DS is willing to thank ICMR (project no. 17X(3)/Adhoc/3/2022-ITR) for the fellowship.

References

1 C. K. Sen, *Adv. Wound Care*, 2019, **8**, 39–48.
2 I. Pastar, O. Stojadinovic, N. C. Yin, H. Ramirez, A. G. Nusbaum, A. Sawaya, S. B. Patel, L. Khalid, R. R. Isseroff and M. Tomic-Canic, *Adv. Wound Care*, 2014, **3**, 445–464.
3 J. E. Janis and B. Harrison, *Plast. Reconstr. Surg.*, 2016, **138**, 9S–17S.
4 P. H. Wang, B. S. Huang, H. C. Horng, C. C. Yeh and Y. J. Chen, *J. Chin. Med. Assoc.*, 2018, **81**, 94–101.
5 Y. Yang, J. Wang, S. Huang, M. Li, J. Chen, D. Pei, Z. Tang and B. Guo, *Natl. Sci. Rev.*, 2024, nwae044.
6 T. N. Demidova-Rice, M. R. Hamblin and I. M. Herman, *Adv. Skin Wound Care*, 2012, **25**, 304–314.
7 A. Sood, M. S. Granick and N. L. Tomaselli, *Wound*, 2014, **3**, 511–529.
8 R. G. Frykberg and J. Banks, *Adv. Wound Care*, 2015, **4**, 560.
9 J. Dworzański, M. Strycharz-Dudziak, E. Kliszczewska, M. Kiełczykowska, A. Dworzańska, B. Drop and M. Polz-Dacewicz, *PLoS One*, 2020, **15**, e0230374.
10 A. Lima, T. Illing, S. Schliemann and P. Elsner, *Am. J. Clin. Dermatol.*, 2017, **18**, 541–553.
11 J. H. Kim, N. Y. Yoon, D. H. Kim, M. Jung, M. Jun, H. Y. Park, C. H. Chung, K. Lee, S. Kim, C. S. Park, K. H. Liu and E. H. Choi, *Exp. Dermatol.*, 2018, **27**, 815–823.
12 H. Wu, F. Li, W. Shao, J. Gao and D. Ling, *ACS Cent. Sci.*, 2019, **5**, 477–485.
13 Y.-K. Wu, N.-C. Cheng and C.-M. Cheng, *Trends Biotechnol.*, 2019, **37**, 505–517.
14 Y. Yang, M. Li, G. Pan, J. Chen and B. Guo, *Adv. Funct. Mater.*, 2023, **33**, 2214089.
15 K. Attri, D. Sharda, B. N. Chudasama, R. Mahajan and D. Choudhury, *RSC Sustainability*, 2023, **1**, 1109–1124.
16 N. Naderi, D. Karponis, A. Mosahebi and A. M. Seifalian, *Front. Biosci.*, 2018, **23**, 1038–1059.

17 S. K. Nethi, S. Das, C. R. Patra and S. Mukherjee, *Biomater. Sci.*, 2019, **7**, 2652–2674.
18 W. Qin, Y. Wu, J. Liu, X. Yuan and J. Gao, *Int. J. Nanomed.*, 2022, 6007–6029.
19 D. Sharda, K. Attri and D. Choudhury, *Antimicrob. Dressings*, 2023, 229–246.
20 D. Sharda and D. Choudhury, *RSC Adv.*, 2023, **13**, 20321–20335.
21 D. Sharda, P. Kaur and D. Choudhury, *Discovery Nano*, 2023, **18**, 127.
22 A. Behera, B. Mittu, S. Padhi, N. Patra and J. Singh, *Multi-functional hybrid nanomaterials for sustainable agri-food and ecosystems*, Elsevier, 2020, pp. 639–682.
23 C. Singh, A. K. Mehata, V. Priya, A. K. Malik, A. Setia, M. N. L. Suseela, Vikas, P. Gokul, Samridhi and S. K. Singh, *Molecules*, 2022, **27**, 7059.
24 A. Sathiyaseelan, K. Saravanakumar and M.-H. Wang, *Int. J. Biol. Macromol.*, 2022, **220**, 1556–1569.
25 A. Zaleska-Medynska, M. Marchelek, M. Diak and E. Grabowska, *Adv. Colloid Interface Sci.*, 2016, **229**, 80–107.
26 H. Fan, Z. Tong, Z. Ren, K. Mishra, S. Morita, E. Edouarzin, L. Gorla, B. Averkiev, V. W. Day and D. H. Hua, *J. Org. Chem.*, 2022, **87**, 6742–6759.
27 X. Yuan, X. Dou, K. Zheng and J. Xie, *Part. Part. Syst. Charact.*, 2015, **32**, 613–629.
28 A. Sannigrahi, S. Chowdhury, I. Nandi, D. Sanyal, S. Chall and K. Chattopadhyay, *Nanoscale Adv.*, 2019, **1**, 3660–3669.
29 F. Paladini and M. Pollini, *Materials*, 2019, **12**, 2540.
30 S. H. Lee and B.-H. Jun, *Int. J. Mol. Sci.*, 2019, **20**, 865.
31 G. Sandri, D. Miele, A. Faccendini, M. C. Bonferoni, S. Rossi, P. Grisoli, A. Taglietti, M. Ruggeri, G. Bruni and B. Vigani, *Polymers*, 2019, **11**, 1207.
32 S. Alizadeh, B. Seyedalipour, S. Shafieyan, A. Kheime, P. Mohammadi and N. Aghdami, *Biochem. Biophys. Res. Commun.*, 2019, **517**, 684–690.
33 J. Salvo and C. Sandoval, *Burns Trauma*, 2022, **10**, tkab047.
34 A. P. Kornblatt, V. G. Nicoletti and A. Travaglia, *J. Inorg. Biochem.*, 2016, **161**, 1–8.
35 A. Das, V. Sudhahar, G.-F. Chen, H. W. Kim, S.-W. Youn, L. Finney, S. Vogt, J. Yang, J. Kweon and B. Surenkhuu, *Sci. Rep.*, 2016, **6**, 33783.
36 Y. Mi, L. Zhong, S. Lu, P. Hu, Y. Pan, X. Ma, B. Yan, Z. Wei and G. Yang, *J. Ethnopharmacol.*, 2022, **290**, 115066.
37 G. Yin, Z. Wang, Z. Wang and X. Wang, *Exp. Dermatol.*, 2018, **27**, 779–786.
38 P. Kaur and D. Choudhury, *J. Drug Target.*, 2021, **29**, 541–550.
39 D. Sharda, K. Attri, P. Kaur and D. Choudhury, *RSC Adv.*, 2021, **11**, 24656–24668.
40 P. Kaur, A. K. Sharma, D. Nag, A. Das, S. Datta, A. Ganguli, V. Goel, S. Rajput, G. Chakrabarti, B. Basu and D. Choudhury, *Nanomedicine*, 2019, **15**, 47–57.
41 M. Hrynyk and R. J. Neufeld, *Burns*, 2014, **40**, 1433–1446.
42 D. Sharda, S. Ghosh, P. Kaur, B. Basu and D. Choudhury, *Discovery Nano*, 2023, **18**, 154.
43 P.-F. Chen, C.-L. Liu, W.-K. Lin, K.-C. Chen, P.-T. Chou and S.-W. Chu, *Biomed. Opt. Express*, 2015, **6**, 3066.
44 F. Tasca and R. Antiochia, *Nanomaterials*, 2020, **10**, 909.
45 T. Odatsu, S. Kuroshima, A. Shinohara, A. Valanezhad and T. Sawase, *Int. J. Biol. Macromol.*, 2021, **190**, 368–374.
46 A. K. Keshari, R. Srivastava, P. Singh, V. B. Yadav and G. Nath, *J. Ayurveda Integr. Med.*, 2020, **11**, 37–44.
47 O. M. Ali, A. A. Bekhit, S. N. Khattab, M. W. Helmy, Y. S. Abdel-Ghany, M. Teleb and A. O. Elzoghby, *Colloids Surf., B*, 2020, **188**, 110824.
48 S. Moniri, M. Ghoranneviss, M. R. Hantehzadeh and M. A. Asadabad, *Bull. Mater. Sci.*, 2017, **40**, 37–43.
49 G. I. N. Waterhouse, G. A. Bowmaker and J. B. Metson, *Phys. Chem. Chem. Phys.*, 2001, **3**, 3838–3845.
50 M. Trivedi, A. Branton, D. Trivedi, G. Nayak, K. Bairwa and S. Jana, *Chromatography Separation Techniques*, 2015, **6**, 1000282.
51 M. H. Habibi and Z. Rezvani, *Spectrochim. Acta, Part A*, 2014, **130**, 309–312.
52 A. J. Kora and J. Arunachalam, *J. Nanomater.*, 2012, **2012**, 1–8.
53 D. Li, Z. Zhang, X. Wang, Y. Wang, X. Gao and Y. Li, *Biosens. Bioelectron.*, 2022, **200**, 113907.
54 A. Bankapur, R. S. Krishnamurthy, E. Zachariah, C. Santhosh, B. Chougule, B. Praveen, M. Valiathan and D. Mathur, *PLoS One*, 2012, **7**, e35075.
55 S. Luber, *J. Phys. Chem. A*, 2013, **117**, 2760–2770.
56 M. Beg, A. Maji, A. K. Mandal, S. Das, M. N. Aktara, P. K. Jha and M. Hossain, *J. Mol. Recognito.*, 2017, **30**, e2565.
57 M. Correia, M. T. Neves-Petersen, P. B. Jeppesen, S. Gregersen and S. B. Petersen, *PLoS One*, 2012, **7**, e50733.